BEILSTEIN ARCHIVES

This open access document is posted as a preprint in the Beilstein Archives at https://doi.org/10.3762/bxiv.2025.31.v1 and is considered to be an early communication for feedback before peer review. Before citing this document, please check if a final, peer-reviewed version has been published.

This document is not formatted, has not undergone copyediting or typesetting, and may contain errors, unsubstantiated scientific claims or preliminary data.

Preprint Title	Understanding the origin of stereoselectivity in the photochemical denitrogenation of 2,3-diazabicyclo[2.2.1]heptene and its derivatives with non-adiabatic molecular dynamics
Authors	Leticia Adao Gomes and Steven A. Lopez
Publication Date	05 May 2025
Article Type	Full Research Paper
Supporting Information File 1	SI_DBH_Final.docx; 1.1 MB
ORCID® iDs	Leticia Adao Gomes - https://orcid.org/0009-0008-7814-6823; Steven A. Lopez - https://orcid.org/0000-0002-8418-3638

License and Terms: This document is copyright 2025 the Author(s); licensee Beilstein-Institut.

This is an open access work under the terms of the Creative Commons Attribution License (https://creativecommons.org/licenses/by/4.0). Please note that the reuse, redistribution and reproduction in particular requires that the author(s) and source are credited and that individual graphics may be subject to special legal provisions. The license is subject to the Beilstein Archives terms and conditions: https://www.beilstein-archives.org/xiv/terms.
The definitive version of this work can be found at https://doi.org/10.3762/bxiv.2025.31.v1

Title: Understanding the origin of stereoselectivity in the photochemical denitrogenation of 2,3-diazabicyclo[2.2.1]heptene and its derivatives with non-adiabatic molecular dynamics.

Leticia A. Gomes and Steven A. Lopez*
Department of Chemistry and Chemical Biology, Northeastern University, Boston, Massachusetts, 02115, United States

Corresponding author: s.lopez@northeastern.edu

Abstract

Photochemical denitrogenation reactions of bicyclic azoalkanes produce strained bicyclic compounds of interest to synthetic organic chemists. We report a computational study on the mechanism of diazabicyclo[2.2.1]heptenes to address long standing mechanistic questions. Indeed, the mechanism of these reactions have been disputed for over six decades. We employed non-adiabatic molecular dynamics (NAMD) simulations combined with state-of-the-art multireference quantum mechanical calculations to understand the photophysical properties and mechanisms of these diazabicyclo[2.2.1]heptenes. The energetically accessible lowest excitations are $n_{NN}(\sigma_{CN}) \rightarrow \pi^*$ and range from 3.94 – 3.97 eV. From the >292 trajectories, the reaction proceeds through a dynamically concerted but asynchronous denitrogenation reactions. One σ_{CN} bond breaks along the S_1-surface; the other σ_{CN} breaks after hopping to the S_0. We identified two clusters of S_1/S_0 surface hopping points from these trajectories. In the first cluster, the methylene bridge is fully inverted relative to the reactant geometry. In the second cluster, the inversion is only partial, with one of the carbon atoms in the methylene bridge inverted relative to the reactant. We identified each cluster's corresponding minimum energy conical intersection (MECI), indicating at least two possible S_1/S_0-MECIs. Our dynamics simulations illustrate that inversion begins in the excited state immediately after the first σ_{CN} bond breaks. This inversion is driven by the atomic momenta acquired after the bond breaks. These dynamical effects promote the formation of the inverted housane, thereby explaining the observed selectivities. A minority of trajectories undergo thermal conversion in the ground state, producing the minor retained housane product from inverted housane.

Keywords

Photochemistry; non-adiabatic molecular dynamics; quantum mechanical calculations; stereoselectivity

Introduction

Photochemical reactions utilize light as a sustainable energy source and are considered to be a 'green' reagent[1, 2]. Organic chromophores absorb light, accessing high-lying excited state(s) that exhibit distinct reactivities, leading to bond breaking and formation, irreversibly producing energy-dense compounds.[2, 3] One promising strategy to access strained compounds involves gas-evolution (e.g., CO or N_2) because of the associated entropic driving force; this approach has had wide utility in photomedicine and organic synthesis. For example, photochemical decarboxylation has been employed to release carbon monoxide at relatively safer doses in biological systems using photoresponsive CO-releasing molecules (photo-CORMs)[4] because have shown anti-inflammatory activity[5, 6]. Photochemical denitrogenation of azoalkanes has been utilized in the stereoselective synthesis of strained compounds such as bicyclo [1.1.0]butane (BCB) and bicyclo [2.1.0]pentane (housane).

Scheme 1. Applications of bicyclo[1.1.0]butane (a) and bicyclo[2.1.0]pentane (b). Molecules with biological activity are synthesized from bicyclo[1.1.0]butane (c) and bicyclo[2.1.0]pentane (d).

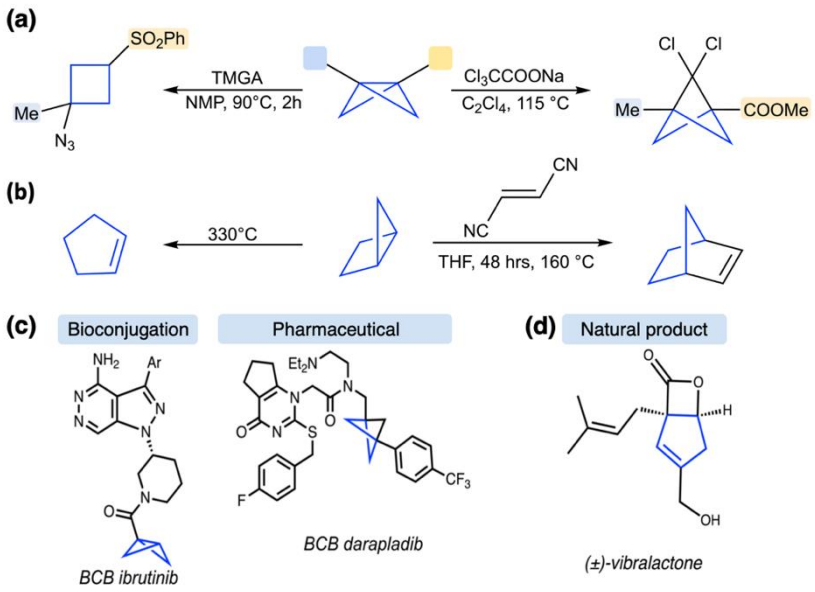

The energy stored in strained σ_{CC} bonds of BCB and housane makes them important building blocks in the synthesis of complex molecular structures. BCBs have been employed in ring-opening reactions with nucleophiles[7-11], radicals[12-15] and electrophiles[16-18] to give cyclobutanes and cyclobutenes[19, 20], which are building blocks in regio- and stereoselective synthesis[21-27] (Scheme 1-a). Additionally, BCB has been used in bioconjugation due to its high chemoselective for cysteine alkylation under mild conditions, for example, BCB-ibrutinib [28] (Scheme 1-c). BCB are also used as a precursor to byciclo[1.1.1]pentanes, which are valuable motifs in drug design[19, 20, 29-33], such as BCP-darapladib (Scheme 1-c).[30, 31, 34-36] Housanes are versatile starting material in different types of reactions including thermal isomerization to cyclopentene[37-39] and 1,4-petadiene[38, 39], chemical electron transfer oxidations to cyclopentene[40] and cycloaddition reactions with electron deficient alkenes and alkynes[39, 41, 42] (Scheme 1-b). Housane derivatives were used in an atom-economical synthesis of the antibiotic [43-45] and potentially anti-obesity drug[46-50], (±)-vibralactone[43] (Scheme 1-d).

Scheme 2. Diastereoselectivity in the Direct Photolysis of 2,3-Diazabicyclo[2.2.1]hept-2-enes

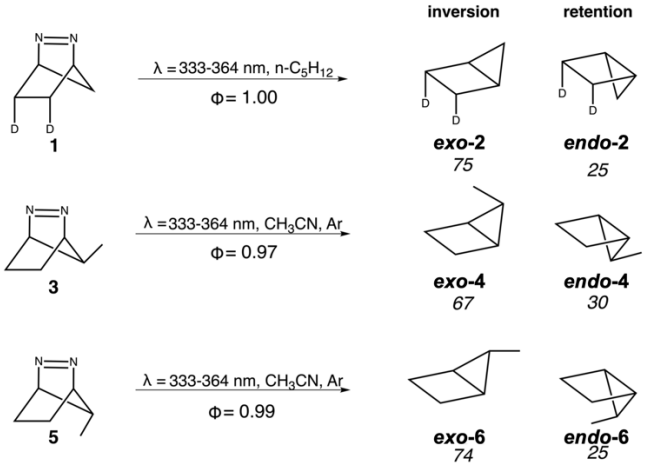

The thermolysis[51-62] and photolysis[59, 60, 62-80] mechanisms of cyclic azoalkenes have been studied with experimental and computational techniques for more than six decades, in solution[52, 56, 61-63, 66, 69, 71, 72, 75-78, 80], gas phase[51, 56, 64, 66, 67], and solid-state [62, 65]. The experimental studies on the thermal denitrogenation of diazabicyclo[2.1.1]hep-2-ene (DBH, **1**) indicate that both the parent compound and its derivatives undergo a concerted elimination of N_2 and the inverted product (***exo*-2**) is preferentially formed [56, 57] In 1965, Crawford and coworkers experimentally found kinetic evidence for a 1,3-diradical from the thermal decomposition of **1**.[57] In 1963, Steel investigated the photolysis of diazabicyclo[2.1.1]hep-2-ene in solution, and the products were the same as thermolysis, nitrogen and bicyclo[2.1.0]pentane with quantum yield approaching unity[66]. Engel and co-workers explored further the reaction using transient spectroscopic methods and discovered that the rate of N_2-formation is significantly slower than that the S_1 fluorescence decay, suggesting that the N_2 is not released at S_1 state [81]. Roth and co-workers discovered a preference to form the inverted product *exo*-2 from deuterated diazabicyclo [2.1.1]hex-2-ene (**1**) (Scheme 2)[73]. Adam and co-workers performed photochemical reactions with derivatives of **1**, including **3** and **5** (Scheme 2) through direct photolysis and benzophenone photosensitizer. No diastereomeric excess was observed[74] for reactions with photosensitizer. Trofimov and co-workers reported the temperature and solvent effect on the stereoselectivities[75-78] and observed a general preference for inversion across several derivatives of **1**[79, 80]. These studies suggest that the thermal denitrogenation of diazabicyclo[2.1.1]hep-2-ene undergoes a concerted elimination of nitrogen mechanism, while the photochemical reaction proceeds with a stepwise mechanism.

Scheme 3. Mechanism for photoenitrogenation of DBH proposed in the literature

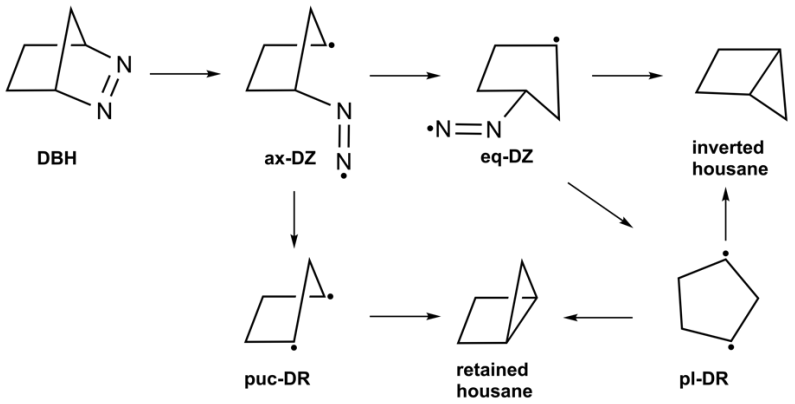

Quantum mechanical calculations have provided valuable insights into the photochemical stereoselectivities of cyclic azoalkenes. In 1998, Olivucci and Robb investigated the reaction paths for α C-N and β C-C cleavage during the direct and sensitized photolysis of **DBH**.[82] The minimum energy geometries in S_0, S_1, T_1, and T_2, conical intersections, transition structures, and singlet/triplet crossing were computed using CASSCF(10,8)/6-31G(d)//MP2/6-31G(d).[82] The results suggested a stepwise C-N breaking with the formation of the diazenyl diradical intermediate.[82] In 2003, Olivucci and his co-workers investigated the inversion stereoselectivity of housane formation using CASPT2(12,10)/6-31G(d)//CASSCF(12,10)/6-31G(d). They also used a single classical trajectory with UB3LYP/6-31G(d) to probe the ground state relaxation dynamics immediately after the conical intersection. They find that axial diazenyl diradical (**ax-DZ** on scheme 3) is selectively generated through a linear-axial conical intersection, providing access to five different reaction pathways. The computed energetics show a production of a cyclopentane-1,3-diyl diradical with a 1:1 production of retained and inverted housane, which disagrees with experimental observations. They argue that the DZ-intermediate reacts before thermal equilibration. The formation of inverted housane occurs via the pseudo-axial-to-equatorial inversion of DZ. From the axial DZ, the puckered-DR (**puc-DR** on scheme 3) radical could be formed resulting in retained housane. From equatorial-DZ (**eq-DZ** on scheme 3), the inverted housane can be through homolytic substitution

(S_H2) process or can form planar-DR (**pl-DR** on scheme 3) radical which afford retained and inverted housane.[83]

Rollins and coworkers also investigated the diradical pathways resulting from thermal decomposition in 2020 using UM06-2X/6-31G(d,p) with quasiclassical trajectories and machine learning analysis.[84] The results suggested a correlation between the out-of-plane bending of the methylene bridge and the stereoselectivity of the formation of retained and inverted housane.[85] Li and co-workers explored the potential energy surfaces and surface crossing points of 2,3-diazabicyclo[2.1.1]hex-2-ene with CASPT2(12,10)/6-31G(d)//CASSCF(12,10)/6-31G(d,p) in 2006 and concluded that on the S_1 surface one C-N bond is broken.[86] In 2011, Abe and co-workers investigated the denitrogenation mechanism of 7,7-diethoxy-2,3-diazabicyclo[2.2.1]hept-2-ene, showing that stepwise C-N bond cleavage is energetically favored using broken-symmetry (BS)-(U)CCSD/6-31G(d) and suggested that an equatorial conformation of the diazinyl diradical leads to the formation of the inverted product. An alternative route via an axial conformation of diazinyl diradical for the inverted product was suggested using Born–Oppenheimer molecular dynamics.[87] Most recently, our group performed multireference calculations with CASPT2(8,8)/ANO-S-VDZP//CASSCF(8,8)/ANO-S-VDZP and non-adiabatic molecular dynamics (NAMD) simulations of a series of diazabicyclo[2.1.1]hexenes. The minimum energy path showed stepwise σ_{CN} bond breaking and led directly to a minimum energy crossing point, corresponding to the inversion product. We also performed NAMD simulations on halogenated derivatives to test the role of hyperconjugative interactions; the NAMD simulations revealed that this stereoelectronic effect substantially perturbs the potential energy surface toward the retention products.[88]

However, for 2,3-diazabicyclo[2.2.1]hept-2-enes, current theoretical reports only offer qualitative mechanistic understanding. The previous studies omit dynamical effects in the photochemical denitrogenation; the overall mechanism and origin of stereoselectivity are still unknown. We use state-of-the-art computations and NAMD simulations to understand the origin of the reactivities and stereoselectivities for a series of 2,3-diazabicyclo[2.2.1]hept-2-enes (Scheme 2). This report shows the first multiconfigurational NAMD simulations studies to understand the photochemical denitrogenation mechanism of 2,3-diazabicyclo[2.2.1]hept-2-enes.

Results and Discussion

We started our studies on characterizing the photophysical properties of **1**, **3**, and **5**. We considered the molecular orbitals and electrons most critical for describing the electronic structure of the molecules in the reaction. The CASSCF[89]/ANO-S-VDZP[90] active space for **1** is shown in Figure 1; we considered 8 electrons and 9 orbitals, along with their average occupancies. For derivatives **3** and **5** with a methyl substituent, the active space also consisted of 8 electrons and 9 orbitals, with their active space and occupancies available in the SI.

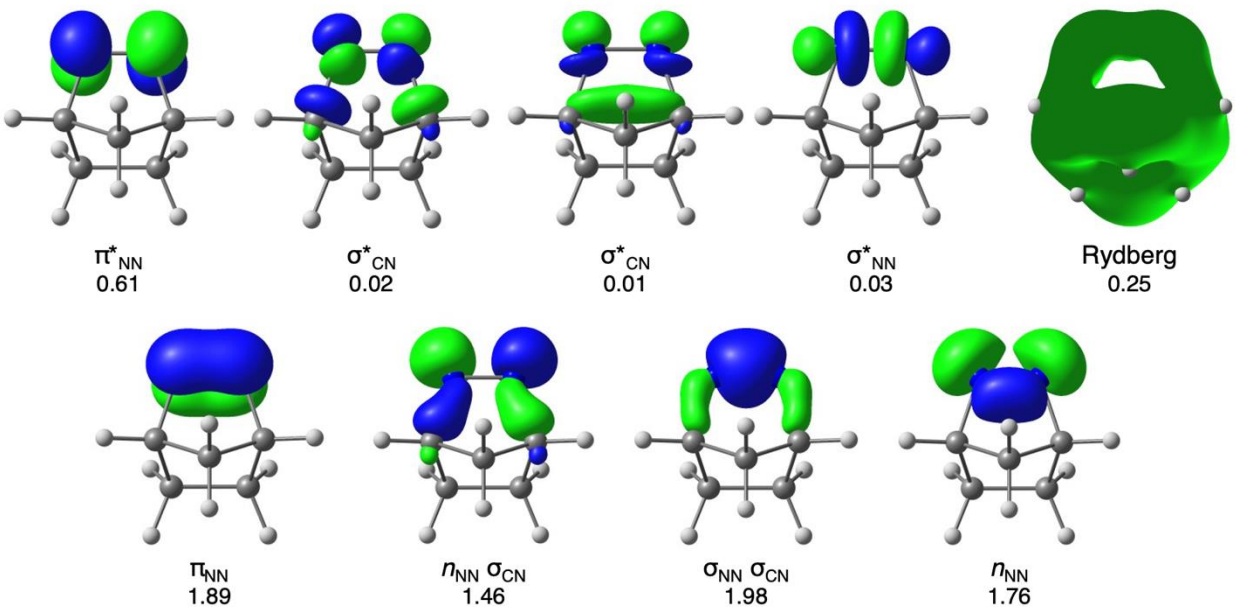

Figure 1. CASSCF(8,9) active space of **1** with average electron occupancies. Orbitals were calculated at the SA(4)-CASSCF(8,9)/ANO-S-VDZP level of theory. An isosurface value of 0.085 was used for all orbitals except Rydberg orbital, whose isosurface is 0.001.

We benchmarked the vertical excitation energy with a (8,9)-active space against those obtained with time-dependent density functional theory by computing the vertical excitation energy, oscillator strength, and nature of the electronic transition of **1**, **3**, and **5** with ωB97X-D[91]/aug-cc-pVTZ[92], SA(4)-CASSCF(8,9)/ANO-VDZP, and SA(4)-XMS-CASPT2[93](8,9)/ANO-S-VDZP levels of theory, as shown in Table 1.

Table 1. Vertical excitation energies, oscillator strengths, and electronic transitions for the first three excited states of **1**, **3**, and **5** at TD-DFT, CASSCF, and XMS-CASPT2 levels of theory.

Molecule	Method	State	Energy (eV)	Wavelength (nm)	Oscillator strength	Nature
1	ωB97X-D/ aug-cc-pVTZ	S_1	3.58	346	0.001	$n_{NN}(\sigma_{CN}) \rightarrow \pi^*$
		S_2	6.23	199	0.001	$n_{NN} \rightarrow \pi^*$
		S_3	6.34	195	0.013	$n_{NN}(\sigma_{CN}) \rightarrow$ Ryd
	XMS-CASPT2(8,9)/ ANO-S-VDZP	S_1	3.97	312		$n_{NN}(\sigma_{CN}) \rightarrow \pi^*$
		S_2	6.13	202		$n_{NN} \rightarrow \pi^*$
		S_3	7.02	177		$n_{NN}(\sigma_{CN}) \rightarrow$ Ryd
	SA4-CASSCF(8,9)/ ANO-S-VDZP	S_1	4.64	267	0.013	$n_{NN}(\sigma_{CN}) \rightarrow \pi^*$
		S_2	6.95	179	0.000	$n_{NN} \rightarrow \pi^*$
		S_3	7.96	156	0.039	$n_{NN}(\sigma_{CN}) \rightarrow$ Ryd
3	ωB97X-D/ aug-cc-pVTZ	S_1	3.56	348	0.000	$n_{NN}(\sigma_{CN}) \rightarrow \pi^*$
		S_2	6.13	202	0.000	$n_{NN} \rightarrow \pi^*$
		S_3	6.38	194	0.008	$n_{NN}(\sigma_{CN}) \rightarrow$ Ryd
	XMS-CASPT2(8,9)/ ANO-S-VDZP	S_1	3.94	315		$n_{NN}(\sigma_{CN}) \rightarrow \pi^*$
		S_2	6.27	198		$n_{NN} \rightarrow \pi^*$
		S_3	7.01	177		$n_{NN}(\sigma_{CN}) \rightarrow$ Ryd
		S_1	4.63	268	0.013	$n_{NN}(\sigma_{CN}) \rightarrow \pi^*$

	SA4-CASSCF(8,9)/ ANO-S-VDZP	S_2	6.92	179	0.000	$n_{NN} \rightarrow \pi^*$
		S_3	8.02	155	0.033	$n_{NN}(\sigma_{CN}) \rightarrow$ Ryd
5	ωB97X-D/aug-cc-pVTZ	S_1	3.55	349	0.001	$n_{NN}(\sigma_{CN}) \rightarrow \pi^*$
		S_2	6.19	200	0.001	$n_{NN} \rightarrow \pi^*$
		S_3	6.31	196	0.008	$n_{NN}(\sigma_{CN}) \rightarrow$ Ryd
	XMS-CASPT2(8,9)/ ANO-S-VDZP	S_1	3.95	314		$n_{NN}(\sigma_{CN}) \rightarrow \pi^*$
		S_2	6.42	193		$n_{NN} \rightarrow \pi^*$
		S_3	7.04	176		$n_{NN}(\sigma_{CN}) \rightarrow$ Ryd
	SA4-CASSCF(8,9)/ ANO-S-VDZP	S_1	4.63	268	0.013	$n_{NN}(\sigma_{CN}) \rightarrow \pi^*$
		S_2	6.96	178	0.000	$n_{NN} \rightarrow \pi^*$
		S_3	8.06	154	0.045	$n_{NN}(\sigma_{CN}) \rightarrow$ Ryd

The $S_0 \rightarrow S_1$ vertical excitation energy, calculated using XMS-CASPT2(8,9)/ANO-S-VDZP, ranges from 3.94 to 3.97 eV and has the electronic transition from $n_{NN}(\sigma_{CN})$ to π*, with an oscillator strength of 0.013 for all molecules. The $S_0 \rightarrow S_2$ excitation involves a $n_{NN} \rightarrow \pi^*$ transition with all methods, and energy with XMS-CASPT2(8,9)/ANO-S-VDZP ranging from 6.13 to 6.42 eV with 0.000 oscillator strength. In contrast, $S_0 \rightarrow S_3$ excitation has a $(\sigma_{CN}) \rightarrow \pi^*$ electronic transition, with energy ranging from 7.01 to 7.04 eV and an oscillator strength ranging from 0.033 to 0.045. These results show agreement between the electronic nature of the transition of TD-DFT, CASSCF, and CASPT2, showing that the chosen active space can capture the photophysics of the molecules.

Table 1 provides photophysical properties for the optimized ground state geometry. However, experimentally, there is an ensemble of non-equilibrium geometries. To get a more realistic understanding of the absorption, we generated 500 geometries using the Wigner-sampling method to generate an ensemble of energetically accessible non-equilibrium geometries. We compute the gas-phase vertical excitation energies ($S_0 \rightarrow S_n$, n = 1, 2, 3) and corresponding oscillator strengths of the Wigner-sampled structures of **1**, **3** and **5** to explore the nature of electronic excitations to the FC regions. This allowed us to predict an absorption spectrum with normalized oscillator strengths ($S_0 \rightarrow S_3$). Figure 3 shows the computed absorption spectrum of **1**, **3**, and **5**.

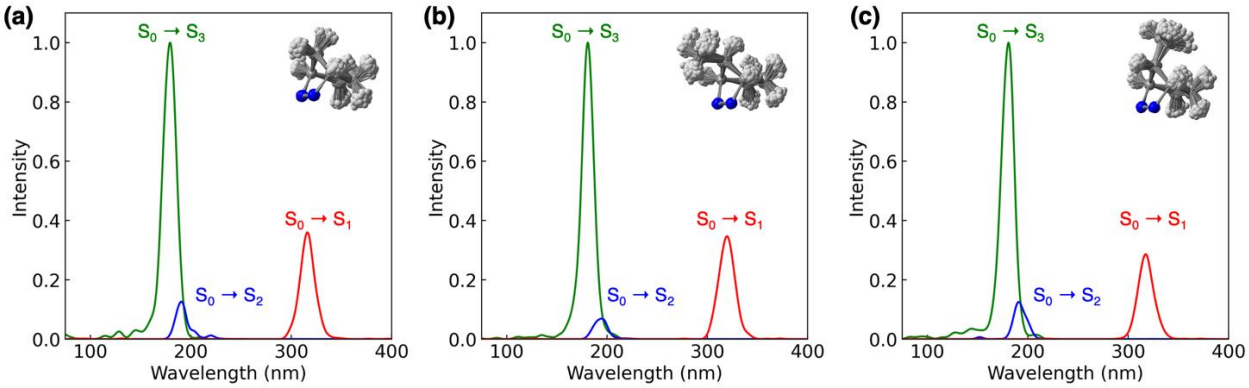

Figure 2: Absorption spectra and geometric overlays corresponding to Wigner sampled geometries of **1** (a), **3** (b), and **5** (c) with XMS-CASPT2(8,9)/ANO-S-VDZP.

Figure 2 shows the **1**, **3**, and **5** computed absorption spectra with three λ^{max} peaks. The S_0 to S_3 has a peak centered from 179 to 181 nm and corresponds to a $n_{NN}(\sigma_{CN}) \rightarrow$ Ryd, the peak centered from 190 to 194 nm corresponds to a majority $n_{NN} \rightarrow \pi^*$ from S_0 to S_2, and the peak centered from 316 to 319 nm corresponds to a majority $n_{NN}(\sigma_{CN}) \rightarrow \pi^*$ from S_0 to S_1. The S_0 to S_3 has the highest intensity due to the

allowed nature of the electronic transition $n_{NN}(\sigma_{CN}) \rightarrow$ Ryd. On the other hand, the S_0 to S_1 peak is expected to have a lower intensity because of the forbidden nature of the $_{NN}(\sigma_{CN}) \rightarrow \pi^*$ electronic transition. This aligns with the trends observed in oscillator strength within the optimized geometry, where the S_0 to S_3 transition shows a higher oscillator strength than the S_0 to S_1 transition. In the case of the S_0 to S_2 transition, the spectrum reveals that a non-equilibrium assembled geometry produced a non-zero oscillator strength, unlike the optimized geometry, which exhibited zero. This difference is attributed to some mixing in the transition nature from S_0 to S_2, involving $n_{NN}(\sigma_{CN}) \rightarrow$ Ryd and $n_{NN} \rightarrow \pi^*$ transitions. The $S_0 \rightarrow S_1$ peaks from 316 to 319 nm are closer to the range of irradiation wavelengths of the experimentally used light source (333-364 nm). For **1**, this peak is closer to experimental absorbance, λ^{max} = 338 nm[81]. The remaining peaks, shown in blue and green for S_2 and S_3, respectively, absorb higher energy than the experimental light source. Electronic transitions to these excited states are impossible in the experiment and thus will not be considered for this photochemical mechanistic study.

DBH photodenitrogenation mechanism

We then turned our attention to the photochemical reaction mechanisms leading to the formation of housane derivatives from 2,3-diazabicyclo[2.2.1]hept-2-enes. To determine the dominant mechanistic pathway, we start with a static exploration with the minimum steepest-descent energy path (MEP) from the FC-point along the S_1 reaction coordinate. Figure 3 shows the MEP and the structure of S_0, the last point of MEP, and S_1 for **1**, **3**, and **5**. These structures are important for understanding the geometrical changes after light absorption and determining the dominant mechanism pathway, along the S_1-reaction coordinate.

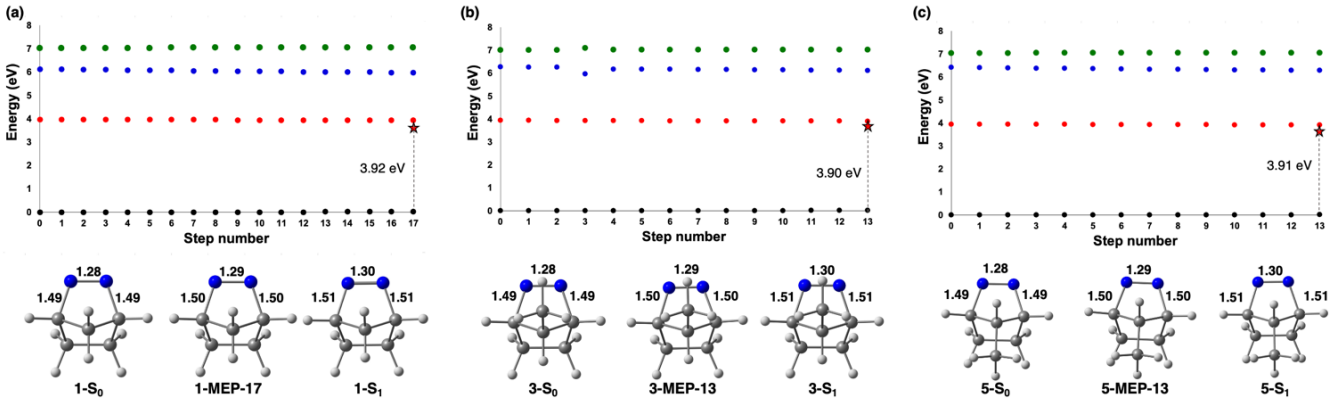

Figure 3. Minimum energy path using XMS-CASPT2(8,9)/ANO-S-VDZP for **1** (a), **3** (b), and **5** (c). The dots on the graphs correspond to the S_0 (black), S_1 (red), S_2 (blue), and S_3 (green) states. Relevant structures (**S_0** and **S_1** minima and endpoints of the **MEP** calculation) are shown below the plots. The C-N and N=N bond lengths are in angstroms on the structures shown. **S_1** energy is shown on the plot with a red star.

The MEP for **1** contains 17 geometries leading to the final structure **1-MEP-17**, and the MEP for **3** and **5** contain 13 geometries leading to final structures **3-MEP-13** and **5-MEP-13**, respectively. The dominant electronic transition is from $n_{NN}(\sigma_{CN}) \rightarrow \pi^*$ for all molecules, and the geometrical changes along the S_1-MEP correspond to an increased population of the π^*_{NN} orbital. In all molecules, the π_{NN} bond length increased from 1.28 Å at S_0 optimized geometry to 1.29 Å at the last MEP structure, which is consistent with the electronic transition because the π_{NN}^* is being populated, resulting in a less stable π_{NN}. The σ_{CN} increased by 0.01 Å along the S_1-MEP for all molecules. The final MEP structure has a large S_1-S_0 energy gap ranging from 3.90 to 3.92 eV with XMS-CASPT2(8,9)/ANO-S-VDZP for all molecules. The large S_1–S_0 energy gap suggests that the dominant mechanistic pathway is toward an S_1-minimum, as it does not indicate a possible crossing between the S_1 and S_0 potential energy surface. We used the last MEP structure

as an input to optimize an S_1 minimum. The S_1 optimized geometries are shown in Figure 3 as **1-S$_1$**, **3-S$_1$,** and **5-S$_1$**. Their energies are 3.83 to 3.87 eV above the S_0 and have nearly identical structure and energy as the last point of the MEP. Based on this static MEP calculation, the experimental quantum yield (**Φ**=0.97-1.00) is inconsistent with this static analysis, since it suggests a non-productive and fluorescence pathway. We hypothesize that these S_1-minima are shallow excited-state minima that can be escaped towards a productive region of the conical intersection seam, or dynamical effects enable this reaction towards near-unity quantum yields. We performed non-adiabatic molecular dynamics (NAMD) simulations starting from the S_1-FC region of **1**, **3**, and **5** to verify our hypotheses, identify the dynamical effects that enable this reaction, and enumerate all possible mechanistic pathways.

Non-adiabatic Molecular Dynamics Simulations

We performed NAMD simulation using the Fewest Switches Surface Hopping (FSSH) algorithm[94-96], implemented with OpenMolcas[97, 98] and integrated with Python Rapid Artificial Intelligence Ab Initio Molecular Dynamics (Pyrai^{2}MD) [99-102] for **1**, **3**, and **5**. The NAMD simulation was performed with the CASSCF(8,9)/ANO-S-VDZP method to elucidate the origin of stereoselectivities and the overall singlet-mediated mechanism involved in denitrogenation. We generated initial conditions with an ensemble of 700 non-equilibrium geometries through Wigner sampling with 300 K velocities. The trajectories were then propagated from the S_1 Franck-Condon region for 1 ps. We defined a complete trajectory as one that reached 1 ps with a maximum energy drift of 0.06 a.u., resulting in 352, 396, and 292 completed trajectories for molecules **1**, **3**, and **5**, respectively; 98-99% of these trajectories end in the S_0.

We wanted first to understand the synchronicity of σ_{CN} bond breaking and whether bond-breaking occurs on the S_1 and/or S_0 state(s). To address these questions, we plotted the two σ_{CN} bond lengths throughout the trajectories (Figure 4). We observe that one σ_{CN} bond breaks first, as indicated by an increase in the σ_{CN} bond length. For the majority of the trajectories, when the broken σ_{CN} bond length reaches 4.5 to 5.0 Å, we observe the breaking of the second bond, suggesting a sequential bond-breaking process. This observation aligns with previous computational studies on the photodenitrogenation of DBH. The black dots represent the hopping points, the geometries where the trajectory crosses from S_1 to S_0. Figure 4 shows that the first σ_{CN} bond breaks on the S_1-surface, while the second σ_{CN} bond breaks after relaxation to S_0. We determine that the denitrogenation is stepwise but on an ultrafast timescale, making it dynamically concerted. By analyzing the state population of the trajectories over time, the obtained time constants were 174 fs for **1**, 163 fs for **3,** and 201 fs for **5**. The plots are available in the supplementary information.

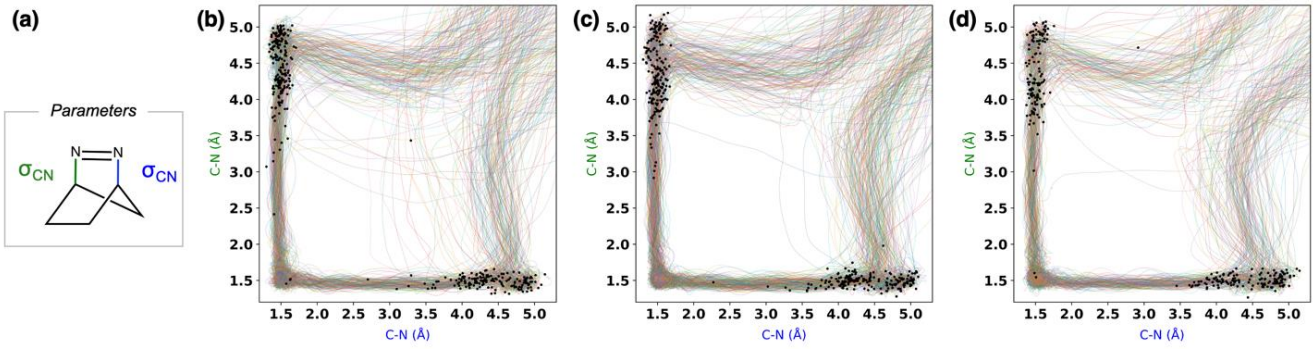

Figure 4. (a) The bond lengths we calculated are depicted. σ_{CN} bonds plotted against each other for **1** (b), **3** (c), and **5** (d). The solid multicolor lines on each plot show the bond lengths over time, and the dots represent the S_1/S_0 surface hopping points for each trajectory.

Next, we aim to elucidate the reaction pathways originating from the S_1 Franck-Condon region for **1**, **3**, and **5**. We classify the final geometries of each trajectory to identify the resulting products and compute their respective quantum yields (QYs). We identify four pathways following the S_1 to S_0 crossing: the reversal to reactant, the inversion product (*exo*), the retention product (*endo*), and a diradical intermediate, as shown in Figure 4. Each pathway is shown in a different color, with the products shown at the bottom in their corresponding colors along with the quantum yields. Our computations indicate high photodenitrogenation quantum yields, ranging from 0.98 to 0.99, which align closely with the experimental QYs observed between 0.97 and 1.00. Some trajectories terminated prematurely at a diradical intermediate. We attempted to extend these trajectories by an additional 0.5 ps; however, most encountered convergence failures or exhibited energy drift exceeding 0.06 a.u. In the one case where the trajectory successfully reached 1.5 ps with conserved energy, we observed the formation of both inverted and retained housane, consistent with the existence of an intermediate. Nevertheless, due to the challenges in consistently achieving 1.5 ps extensions while maintaining energy conservation, these trajectories were excluded from the statistical analysis of the housane quantum yield.

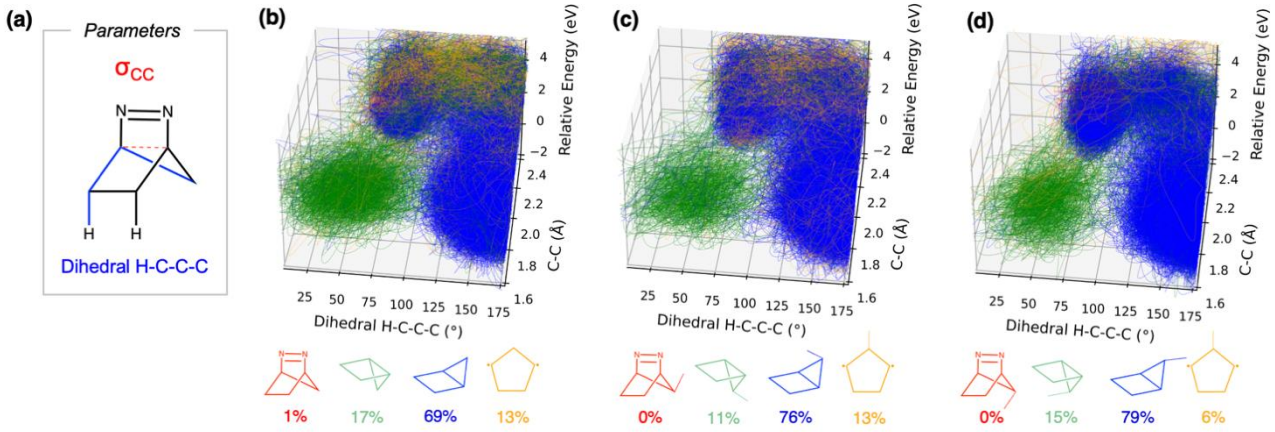

Figure 5. (a) Geometrical parameters. Plots show trajectories for a 1 ps NAMD simulation with CASSCF (8,9)/ANO-S-VDZP, monitoring C-C bond formation, H-C-C-C dihedral angle, and relative energy for **1** (b), **3** (c), and **5** (d). The energy is relative to the lowest total energy of each trajectory. The red trajectories return to reactant, the green trajectories form retained housane, the blue trajectories form inverted housane, and the yellow trajectories lead to a diradical intermediate. The quantum yield for each species is provided below its structure.

The inverted housane exhibited the highest quantum yields, ranging from 0.69 to 0.79, consistent with the experimentally observed preferred product. Notably, all trajectories leading to retained housane passed through the region associated with inverted housane, characterized by dihedral angles exceeding 110°. This observation offers new insights into the reaction mechanism, showing that inverted housane forms initially in the ground state and can thermally convert into retained housane. This finding represents a significant shift in mechanistic understanding, highlighting the importance of incorporating dynamical effects. Previous studies, summarized in Scheme 3, predicted that a diazenyl diradical (**az-DZ**) with one broken C–N bond would retain the stereochemistry of the reactant, leading directly to the formation of retained housane. However, this pathway was not observed when dynamical effects were included in our simulations. Our predicted inverted to retained housane ratios — 4, 7, and 5 for **1**, **3**, and **5**, respectively — are higher than the experimental ratios of 3, 2, and 3. We attribute this overestimation to the limited simulation time of 1 ps. Since retained housane forms via thermal conversion from inverted housane, longer timescales are likely required to capture its formation accurately. Nevertheless, we maintained the 1 ps simulation length to ensure energy conservation, as energy drift increases with longer trajectory times, and to obtain a statistically representative number of trajectories.

We analyze the S_1/S_0 crossing by examining the geometries of the hopping points to understand the stereoselectivities of the inverted housanes. We plotted the two H-C-C-C dihedral angles, shown in Figure 6a, and estimated the local density for each hopping point using kernel density estimation, as shown in Figures 6b-d. By plotting the dihedral angles, we identified two types of hopping points: one that is partially inverted and another that is fully inverted. The H-C-C-C dihedral angles of the reactant optimized geometry range from 81° to 83° for compounds **1**, **3**, and **5**. By plotting the dihedral, two types of hopping points were identified. The first type, termed partially inverted hopping point, features one dihedral angle similar to that of the reactant, ranging from 60° to 90° across all molecules. In contrast, the other dihedral angle is significantly larger, with the highest density localized between 140° and 160°, 130° and 150°, and 120° and 140° for compounds **1**, **3**, and **5**, respectively. The lower dihedral angle ranges observed for the largest dihedral angle for derivatives **3** and **5** suggest that the methyl substituent on the methylene group restricts dihedral inversion. This restriction may arise from increased steric hindrance imposed by the methyl group on the methylene bridge of the derivatives. Two clusters represent the partially inverted hopping point, depending on which σ_{CN} breaks first. The second type, referred to as the inverted hopping point, occurs when both dihedral angles are significantly larger than those of the reactant, with both dihedral angles ranging from 140° and 160°, 130° and 150°, and 120° and 140° for compounds **1**, **3**, and **5**.

We selected representative trajectories from **1** to illustrate different types of hopping points. **Figure 6f** shows snapshots from a trajectory that leads to a partially inverted hopping point. At 1 fs, both dihedral angles are similar, with θ_1 at 87° and θ_2 at 89°. By 150 fs, the first σ_{CN} bond breaks. The dihedral angle θ_2, corresponding to the carbon still bonded to N_2, increases to 109°, while θ_1 rises slightly to 90°. At the hopping point (276 fs), θ_1 remains nearly unchanged at 88°, but θ_2 increases significantly to 155°, indicating that the carbon bonded to N_2 is already inverted and positioned above the molecular plane. In contrast, the other carbons are in the plane or below it; we consider this hopping point geometry partially inverted. A trajectory snapshot leading to a fully inverted hopping point is shown in Figure 6. At 1 fs, both dihedral angles are identical at 83°. At 150 fs, the σ_{CN} bond is broken, θ_1 decreases slightly to 72°; θ_2 increases substantially to 132°, placing the carbon bonded to N_2 above the molecule plane. At the hopping point (274 fs), both θ_1 and θ_2 are significantly increased (149° and 153°, respectively). Here, all carbons of the methylene bridge are located above the molecular plane, indicating complete inversion of stereochemistry.

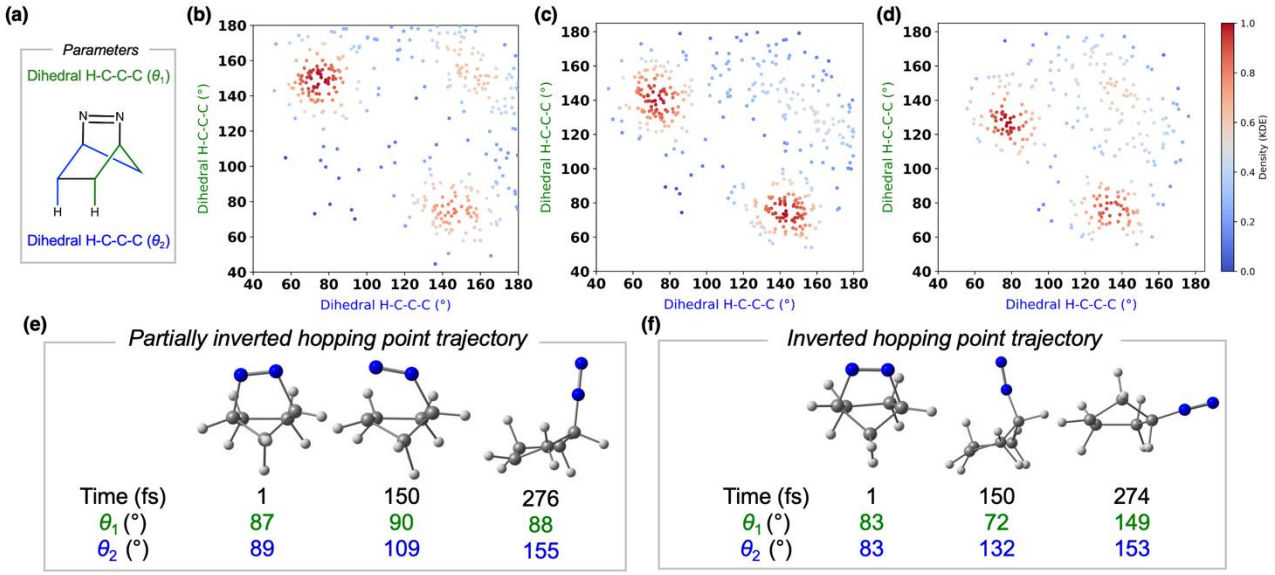

Figure 6. (a) Geometrical parameters. H-C-C-C dihedral angles plotted against each other for S_1 to S_0 hopping point geometry of **1** (b), **3** (c), and **5** (d). Representative trajectories for partially inverted hopping point (e) and completely inverted hopping point (f).

Using kernel density estimation[103], we found that partially inverted hopping points can be found in high-density regions, plotted in red within their respective clusters across all molecules. The observed geometric differences and distinct clustering patterns suggest the existence of two separate $S_1 \rightarrow S_0$ crossing channels. To test this hypothesis and investigate the preference for partially inverted hopping geometries, we performed optimizations of the minimum energy conical intersection (MECI). The MECI for the partially inverted hopping point (**MECI-PI**) and the inverted hopping point (**MECI-I**) for **1**, **3**, and **5** are shown in Figure 7.

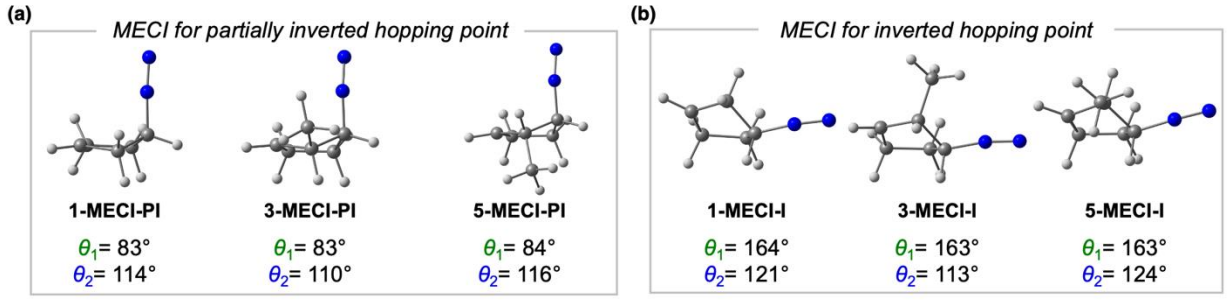

Figure 7. The minimum energy conical intersection geometries are shown for the partially inverted hopping point (a) and the inverted hopping point (b), along with their dihedrals for **1**, **3**, and **5**.

The **MECI-PI** exhibits θ_1 between 83° and 84°, and θ_2, a more elongated dihedral angle, ranging from 110° to 116°. In contrast, **MECI-I** displays two elongated dihedral angles: θ_1 ranges from 163° to 164°, and θ_2 from 113° to 124°. The significant geometrical difference supports the hypothesis of two crossing regions between the S_1 and S_0. The MECI-PI has lower energy for all molecules studied than the MECI-I, by being lower in energy by 0.15 eV, 0.19 eV, and 0.09 eV for **1**, **3**, and **5**, respectively. These results suggest that the gradient towards the **MECI-PI** is steeper than for **MECI-I**, making the pathway to the MECI-PI more favorable. All MECI structures show partial stereochemical inversion. Following the initial σ_{CN} bond cleavage, the carbon atom still bonded to N_2 begins to move towards inversion, indicating that dynamic effects help promote the stereoselective inversion.

Conclusion

We used multiconfigurational quantum mechanical calculations and NAMD simulations to investigate the mechanism of photodenitrogenation of 2,3-diazabicyclo[2.2.1]heptene and its derivatives, which produce strained compound housane, important building blocks in the synthesis of complex molecular structures. We identified that the key electronic transitions are $S_0 \rightarrow S_1$ ($n_{NN}(\sigma_{CN}) \rightarrow \pi^*$) transitions, with excitation energies ranging from 3.94 to 3.97 eV. MEP calculations indicate that the dominant mechanistic pathway leads to an S_1-minimum, which is inconsistent with the nearly unity quantum yield observed experimentally. We employed NAMD to explore all possible mechanistic pathways and identify the dynamic effects that enable this reaction. The predicted quantum yields ranged from 0.98 to 0.99, aligning closely with the experimentally observed quantum yields of 0.97 to 1.00. Our simulations reveal that all productive trajectories involve a dynamically concerted but asynchronous denitrogenation reaction, characterized by breaking one σ_{CN} bond in the S_1-state and the second σ_{CN} bond in the S_0-state. After the first σ_{CN} bond breaks, the stereochemistry of the carbon bonded to N_2 begins to invert, suggesting that dynamic effects promote this inversion. The diazenyl diradical, which shares the same stereochemistry as

the reactant–and was proposed in prior studies–was not observed when dynamic effects were included in our simulations. Following the S_1/S_0 surface hopping points, we identified four distinct pathways: reversion to the reactant, formation of the inversion product *exo*-housanes, formation of the retention products *endo*-housane, and formation of *exo*-housane, which presumably undergoes ring-closing if given sufficient simulation time. These were unfortunately prohibitively expensive due to the CASSCF computation of the energy, gradients, and non-adiabatic couplings at each 0.5 fs timestep. Our results indicate that the retained stereochemistry of housane is generated in the ground state via thermal conversion from retained housane.

Acknowledgements

This work was supported by the National Science Foundation Center CAREER grant (NSF-CHE-2144556). All authors appreciate the assistance from the Northeastern Research Computing Team and the computing resources provided by the Massachusetts Life Science Center grant (G00006360).

Supporting Information

The data supporting this article have been included in the Supplementary Information, which includes a link to access all optimized structures, output files for vertical excitation energy, MEP, and dynamics (including energies, xyz, and velocities for each trajectory). The active space for derivatives, time constants, the outcome of extended trajectories ending at the diradical intermediate, and energy of MECIs.

References

(1) Albini, A.; Fagnoni, M. Green chemistry and photochemistry were born at the same time. *Green Chemistry* **2004**, *6* (1), 1-6, 10.1039/B309592D. DOI: 10.1039/B309592D.
(2) Buglioni, L.; Raymenants, F.; Slattery, A.; Zondag, S. D. A.; Noel, T. Technological Innovations in Photochemistry for Organic Synthesis: Flow Chemistry, High-Throughput Experimentation, Scale-up, and Photoelectrochemistry. *Chem Rev* **2022**, *122* (2), 2752-2906. DOI: 10.1021/acs.chemrev.1c00332.
(3) Ballini, R. 2.1.1 Photochemistry and Green Chemistry. In *Eco-Friendly Synthesis of Fine Chemicals*, Royal Society of Chemistry (RSC).
(4) Singh, P. K.; Mengji, R.; Kumar, S.; Singh, A. K.; Jana, A.; Singh, S. P. BODIPY-Based Mitochondrial Targeted NIR-Responsive CO-Releasing Platform for the On-Demand Release of CO to Treat Cancer. *ACS Appl Bio Mater* **2023**, *6* (9), 3778-3789. DOI: 10.1021/acsabm.3c00440.
(5) Ryter, S. W.; Alam, J.; Choi, A. M. Heme oxygenase-1/carbon monoxide: from basic science to therapeutic applications. *Physiol Rev* **2006**, *86* (2), 583-650. DOI: 10.1152/physrev.00011.2005.
(6) S, R. O.; Queiroga, C. S.; Vieira, H. L. Mitochondria and carbon monoxide: cytoprotection and control of cell metabolism - a role for Ca(2+) ? *J Physiol* **2016**, *594* (15), 4131-4138. DOI: 10.1113/JP270955.
(7) Gaoni, Y.; Tomazic, A.; Potgieter, E. Stereochemistry of addition of organocopper reagents and of the hydride ion to 1-(arylsulfonyl)bicyclo[1.1.0]butanes. *The Journal of Organic Chemistry* **1985**, *50* (16), 2943-2947. DOI: 10.1021/jo00216a027.
(8) Gaoni, Y.; Tomazic, A. Bridgehead reactivity, nucleophilic and radical additions, and lithium aluminum hydride reduction of 1-(arylsulfonyl)bicyclobutanes: general access to substituted, functionalized cyclobutanes. Syntheses of (.+-.)-citrilol acetate, (.+-.)-junionone, and the tricyclo[3.3.0.01,4]octane and tricyclo[4.3.0.01,7]nonane ring systems. *The Journal of Organic Chemistry* **1985**, *50* (16), 2948-2957. DOI: 10.1021/jo00216a028.
(9) Lopchuk, J. M.; Fjelbye, K.; Kawamata, Y.; Malins, L. R.; Pan, C. M.; Gianatassio, R.; Wang, J.; Prieto, L.; Bradow, J.; Brandt, T. A.; et al. Strain-Release Heteroatom Functionalization: Development, Scope, and Stereospecificity. *J Am Chem Soc* **2017**, *139* (8), 3209-3226. DOI: 10.1021/jacs.6b13229.
(10) McNamee, R. E.; Thompson, A. L.; Anderson, E. A. Synthesis and Applications of Polysubstituted Bicyclo[1.1.0]butanes. *J Am Chem Soc* **2021**, *143* (50), 21246-21251. DOI: 10.1021/jacs.1c11244.

(11) Guo, L.; Noble, A.; Aggarwal, V. K. alpha-Selective Ring-Opening Reactions of Bicyclo[1.1.0]butyl Boronic Ester with Nucleophiles. *Angew Chem Int Ed Engl* **2021**, *60* (1), 212-216. DOI: 10.1002/anie.202011739.
(12) Wu, X.; Hao, W.; Ye, K. Y.; Jiang, B.; Pombar, G.; Song, Z.; Lin, S. Ti-Catalyzed Radical Alkylation of Secondary and Tertiary Alkyl Chlorides Using Michael Acceptors. *J Am Chem Soc* **2018**, *140* (44), 14836-14843. DOI: 10.1021/jacs.8b08605.
(13) Silvi, M.; Aggarwal, V. K. Radical Addition to Strained sigma-Bonds Enables the Stereocontrolled Synthesis of Cyclobutyl Boronic Esters. *J Am Chem Soc* **2019**, *141* (24), 9511-9515. DOI: 10.1021/jacs.9b03653.
(14) Ernouf, G.; Chirkin, E.; Rhyman, L.; Ramasami, P.; Cintrat, J. C. Photochemical Strain-Release-Driven Cyclobutylation of C(sp(3))-Centered Radicals. *Angew Chem Int Ed Engl* **2020**, *59* (7), 2618-2622. DOI: 10.1002/anie.201908951.
(15) Ociepa, M.; Wierzba, A. J.; Turkowska, J.; Gryko, D. Polarity-Reversal Strategy for the Functionalization of Electrophilic Strained Molecules via Light-Driven Cobalt Catalysis. *J Am Chem Soc* **2020**, *142* (11), 5355-5361. DOI: 10.1021/jacs.0c00245.
(16) Walczak, M. A.; Krainz, T.; Wipf, P. Ring-strain-enabled reaction discovery: new heterocycles from bicyclo[1.1.0]butanes. *Acc Chem Res* **2015**, *48* (4), 1149-1158. DOI: 10.1021/ar500437h.
(17) Fawcett, A.; Biberger, T.; Aggarwal, V. K. Carbopalladation of C-C sigma-bonds enabled by strained boronate complexes. *Nat Chem* **2019**, *11* (2), 117-122. DOI: 10.1038/s41557-018-0181-x.
(18) Kerner, M. J.; Wipf, P. Semipinacol-Type Rearrangements of [3-(Arylsulfonyl)bicyclo[1.1.0]butan-1-yl]alkanols. *Org Lett* **2021**, *23* (9), 3615-3619. DOI: 10.1021/acs.orglett.1c01004.
(19) Golfmann, M.; Walker, J. C. L. Bicyclobutanes as unusual building blocks for complexity generation in organic synthesis. *Commun Chem* **2023**, *6* (1), 9. DOI: 10.1038/s42004-022-00811-3.
(20) Tyler, J. L.; Aggarwal, V. K. Synthesis and Applications of Bicyclo[1.1.0]butyl and Azabicyclo[1.1.0]butyl Organometallics. *Chemistry* **2023**, *29* (29), e202300008. DOI: 10.1002/chem.202300008.
(21) Namyslo, J. C.; Kaufmann, D. E. The Application of Cyclobutane Derivatives in Organic Synthesis. *Chemical Reviews* **2003**, *103* (4), 1485-1538. DOI: 10.1021/cr010010y.
(22) Bauer, M. R.; Di Fruscia, P.; Lucas, S. C. C.; Michaelides, I. N.; Nelson, J. E.; Storer, R. I.; Whitehurst, B. C. Put a ring on it: application of small aliphatic rings in medicinal chemistry. *RSC Med Chem* **2021**, *12* (4), 448-471. DOI: 10.1039/d0md00370k.
(23) de Nanteuil, F.; De Simone, F.; Frei, R.; Benfatti, F.; Serrano, E.; Waser, J. Cyclization and annulation reactions of nitrogen-substituted cyclopropanes and cyclobutanes. *Chem Commun (Camb)* **2014**, *50* (75), 10912-10928. DOI: 10.1039/c4cc03194f.
(24) Liang, Z.; Wang, L.; Wang, Y.; Wang, L.; Chong, Q.; Meng, F. Cobalt-Catalyzed Diastereo- and Enantioselective Carbon-Carbon Bond Forming Reactions of Cyclobutenes. *J Am Chem Soc* **2023**, *145* (6), 3588-3598. DOI: 10.1021/jacs.2c12475.
(25) Misale, A.; Niyomchon, S.; Maulide, N. Cyclobutenes: At a Crossroad between Diastereoselective Syntheses of Dienes and Unique Palladium-Catalyzed Asymmetric Allylic Substitutions. *Acc Chem Res* **2016**, *49* (11), 2444-2458. DOI: 10.1021/acs.accounts.6b00375.
(26) Xu, Y.; Conner, M. L.; Brown, M. K. Cyclobutane and cyclobutene synthesis: catalytic enantioselective [2+2] cycloadditions. *Angew Chem Int Ed Engl* **2015**, *54* (41), 11918-11928. DOI: 10.1002/anie.201502815.
(27) Fawcett, A. Recent advances in the chemistry of bicyclo- and 1-azabicyclo[1.1.0]butanes. *Pure and Applied Chemistry* **2020**, *92* (5), 751-765. DOI: 10.1515/pac-2019-1007.
(28) Tokunaga, K.; Sato, M.; Kuwata, K.; Miura, C.; Fuchida, H.; Matsunaga, N.; Koyanagi, S.; Ohdo, S.; Shindo, N.; Ojida, A. Bicyclobutane Carboxylic Amide as a Cysteine-Directed Strained Electrophile for Selective Targeting of Proteins. *J Am Chem Soc* **2020**, *142* (43), 18522-18531. DOI: 10.1021/jacs.0c07490.
(29) Stepan, A. F.; Subramanyam, C.; Efremov, I. V.; Dutra, J. K.; O'Sullivan, T. J.; DiRico, K. J.; McDonald, W. S.; Won, A.; Dorff, P. H.; Nolan, C. E.; et al. Application of the bicyclo[1.1.1]pentane motif

as a nonclassical phenyl ring bioisostere in the design of a potent and orally active gamma-secretase inhibitor. *J Med Chem* **2012**, *55* (7), 3414-3424. DOI: 10.1021/jm300094u.
(30) Measom, N. D.; Down, K. D.; Hirst, D. J.; Jamieson, C.; Manas, E. S.; Patel, V. K.; Somers, D. O. Investigation of a Bicyclo[1.1.1]pentane as a Phenyl Replacement within an LpPLA(2) Inhibitor. *ACS Med Chem Lett* **2017**, *8* (1), 43-48. DOI: 10.1021/acsmedchemlett.6b00281.
(31) Bychek, R. M.; Hutskalova, V.; Bas, Y. P.; Zaporozhets, O. A.; Zozulya, S.; Levterov, V. V.; Mykhailiuk, P. K. Difluoro-Substituted Bicyclo[1.1.1]pentanes for Medicinal Chemistry: Design, Synthesis, and Characterization. *J Org Chem* **2019**, *84* (23), 15106-15117. DOI: 10.1021/acs.joc.9b01947.
(32) Locke, G. M.; Bernhard, S. S. R.; Senge, M. O. Nonconjugated Hydrocarbons as Rigid-Linear Motifs: Isosteres for Material Sciences and Bioorganic and Medicinal Chemistry. *Chemistry* **2019**, *25* (18), 4590-4647. DOI: 10.1002/chem.201804225.
(33) Tse, E. G.; Houston, S. D.; Williams, C. M.; Savage, G. P.; Rendina, L. M.; Hallyburton, I.; Anderson, M.; Sharma, R.; Walker, G. S.; Obach, R. S.; et al. Nonclassical Phenyl Bioisosteres as Effective Replacements in a Series of Novel Open-Source Antimalarials. *J Med Chem* **2020**, *63* (20), 11585-11601. DOI: 10.1021/acs.jmedchem.0c00746.
(34) Ma, X.; Sloman, D. L.; Han, Y.; Bennett, D. J. A Selective Synthesis of 2,2-Difluorobicyclo[1.1.1]pentane Analogues: "BCP-F(2)". *Org Lett* **2019**, *21* (18), 7199-7203. DOI: 10.1021/acs.orglett.9b02026.
(35) Ma, X.; Pinto, W.; Pham, L. N.; Sloman, D. L.; Han, Y. Synthetic Studies of 2,2-Difluorobicyclo[1.1.1]pentanes (BCP-F2
): The Scope and Limitation of Useful Building Blocks for Medicinal Chemists. *European Journal of Organic Chemistry* **2020**, *2020* (29), 4581-4605. DOI: 10.1002/ejoc.202000679.
(36) Eaton, P. E.; Daniels, R. G.; Casucci, D.; Cunkle, G. T.; Engel, P. Amide activation for cyclopropane ortho-lithiation. *The Journal of Organic Chemistry* **1987**, *52* (10), 2100-2102. DOI: 10.1021/jo00386a040.
(37) Halberstadt, M. L.; Chesick, J. P. The Kinetics of the Thermal Isomerization of [2.1.0]Bicyclopentane. *Journal of the American Chemical Society* **1962**, *84* (14), 2688-2691. DOI: 10.1021/ja00873a008.
(38) Steel, C.; Zand, R.; Hurwitz, P.; Cohen, S. G. Small Ring Bicyclic Azo Compounds and Bicyclic Hydrocarbons. Isomerization of Bicyclo [2.1.0.] pentane and Bicyclo [2.2.0] hexane. *Journal of the American Chemical Society* **1964**, *86* (4), 679-684. DOI: 10.1021/ja01058a027.
(39) Carpenter, B. K. Understanding the puzzling chemistry of bicyclo[2.1.0]pentane. *Org Biomol Chem* **2004**, *2* (1), 103-109. DOI: 10.1039/b310676d.
(40) Adam, W.; Corma, A.; Miranda, M. A.; Sabater-Picot, M.-J.; Sahin, C. Photochemical and Chemical Electron Transfer Reactions of Bicyclo[2.1.0]pentanes (Housanes) in Solution and in Zeolite Cavities. *Journal of the American Chemical Society* **1996**, *118* (10), 2380-2386. DOI: 10.1021/ja950397k.
(41) Redmond, K.; Carpenter, B. K. A New Thermally Generated Biradical Capable of Intermolecular Hydrogen Atom Abstraction. *The Journal of Organic Chemistry* **1997**, *62* (17), 5668-5669. DOI: 10.1021/jo970791w.
(42) Gassman, P. G.; Mansfield, K. T.; Murphy, T. J. The mechanism and stereochemistry of the addition of olefins to bicyclo[2.1.0]pentane. *Journal of the American Chemical Society* **1968**, *90* (17), 4746-4748. DOI: 10.1021/ja01019a054.
(43) Nistanaki, S. K.; Boralsky, L. A.; Pan, R. D.; Nelson, H. M. A Concise Total Synthesis of (+/-)-Vibralactone. *Angew Chem Int Ed Engl* **2019**, *58* (6), 1724-1726. DOI: 10.1002/anie.201812711.
(44) Böttcher, T.; Sieber, S. A. β-Lactones as Specific Inhibitors of ClpP Attenuate the Production of Extracellular Virulence Factors of Staphylococcus aureus. *Journal of the American Chemical Society* **2008**, *130* (44), 14400-14401. DOI: 10.1021/ja8051365.
(45) Zeiler, E.; Braun, N.; Böttcher, T.; Kastenmüller, A.; Weinkauf, S.; Sieber, S. A. Vibralactone as a Tool to Study the Activity and Structure of the ClpP1P2 Complex from Listeria monocytogenes. *Angewandte Chemie International Edition* **2011**, *50* (46), 11001-11004. DOI: https://doi.org/10.1002/anie.201104391.

(46) Liu, D.-Z.; Wang, F.; Liao, T.-G.; Tang, J.-G.; Steglich, W.; Zhu, H.-J.; Liu, J.-K. Vibralactone: A Lipase Inhibitor with an Unusual Fused β-Lactone Produced by Cultures of the Basidiomycete Boreostereum vibrans. *Organic Letters* **2006**, *8* (25), 5749-5752. DOI: 10.1021/ol062307u.
(47) Wei, K.; Wang, G.-Q.; Bai, X.; Niu, Y.-F.; Chen, H.-P.; Wen, C.-N.; Li, Z.-H.; Dong, Z.-J.; Zuo, Z.-L.; Xiong, W.-Y.; et al. Structure-Based Optimization and Biological Evaluation of Pancreatic Lipase Inhibitors as Novel Potential Antiobesity Agents. *Natural Products and Bioprospecting* **2015**, *5* (3), 129-157. DOI: 10.1007/s13659-015-0062-6.
(48) Zhou, Q.; Snider, B. B. Synthesis of (±)-Vibralactone. *Organic Letters* **2008**, *10* (7), 1401-1404. DOI: 10.1021/ol800118c.
(49) Zhou, Q.; Snider, B. B. Synthesis of (±)- and (−)-Vibralactone and Vibralactone C. *The Journal of Organic Chemistry* **2008**, *73* (20), 8049-8056. DOI: 10.1021/jo8015743.
(50) Leeder, A. J.; Heap, R. J.; Brown, L. J.; Franck, X.; Brown, R. C. D. A Short Diastereoselective Total Synthesis of (±)-Vibralactone. *Organic Letters* **2016**, *18* (23), 5971-5973. DOI: 10.1021/acs.orglett.6b03007.
(51) Chang, M. H.; Dougherty, D. A. Phase-dependent stereochemistry and chemical activation in the thermal decomposition of 2,3-diazabicyclo[2.1.1]hexene. *Journal of the American Chemical Society* **1982**, *104* (4), 1131-1132. DOI: 10.1021/ja00368a053.
(52) Chang, M. H.; Dougherty, D. A. 2,3-Diazabicyclo[2.1.1]hex-2-ene. Synthesis and thermal decomposition. *The Journal of Organic Chemistry* **1981**, *46* (20), 4092-4093. DOI: 10.1021/jo00333a040.
(53) Peterson, T. H.; Carpenter, B. K. Estimation of dynamic effects on product ratios by vectorial decomposition of a reaction coordinate. Application to thermal nitrogen loss from bicyclic azo compounds. *Journal of the American Chemical Society* **1992**, *114* (2), 766-767. DOI: 10.1021/ja00028a057.
(54) Hamaguchi, M.; Nakaishi, M.; Nagai, T.; Nakamura, T.; Abe, M. Notable Effect of an Electron-Withdrawing Group at C3 on the Selective Formation of Alkylidenecyclobutanes in the Thermal Denitrogenation of 4-Spirocyclopropane-1-pyrazolines. Nonstatistical Dynamics Effects in the Denitrogenation Reactions. *Journal of the American Chemical Society* **2007**, *129* (43), 12981-12988. DOI: 10.1021/ja068513e.
(55) Reyes, M. B.; Carpenter, B. K. Mechanism of Thermal Deazetization of 2,3-Diazabicyclo[2.2.1]hept-2-ene and Its Reaction Dynamics in Supercritical Fluids. *Journal of the American Chemical Society* **2000**, *122* (41), 10163-10176. DOI: 10.1021/ja0016809.
(56) Allred, E. L.; Smith, R. L. Thermolysis of exo- and endo-5-methoxy-2,3-diazabicyclo[2.2.1]-2-heptene. *Journal of the American Chemical Society* **1967**, *89* (26), 7133-7134. DOI: 10.1021/ja01002a063.
(57) Crawford, R. J.; Dummel, R. J.; Mishra, A. Kinetic Evidence for 1,3-Diradicals from the Thermal Decomposition of 1-Pyrazolines. *Journal of the American Chemical Society* **1965**, *87* (13), 3023-3025. DOI: 10.1021/ja01091a053.
(58) Fleischer, E. B.; Lavallee, D. Thermolysis of exo- and
endo-5-Methoxy-2,3-diazabicyclo[2.2.1]-heptene. *Journal of the American Chemical Society* **1967**, *89* (26), 7133-7134.
(59) Engel, P. S. Mechanism of the thermal and photochemical decomposition of azoalkanes. *Chemical Reviews* **1980**, *80* (2), 99-150. DOI: 10.1021/cr60324a001.
(60) Adam, W.; Oppenlaender, T.; Zang, G. Photochemistry of the azoalkanes 2,3-diazabicyclo[2.2.1]hept-2-ene and spiro[cyclopropane-7,1'-[2,3]-diazabicyclo[2.2.1]hept-2-ene]: on the questions of one-bond vs. two-bond cleavage during the denitrogenation, cyclization vs. rearrangement of the 1,3-diradicals and double inversion. *The Journal of Organic Chemistry* **1985**, *50* (18), 3303-3312. DOI: 10.1021/jo00218a012.
(61) Chang, M. H.; Jain, R.; Dougherty, D. A. Chemical activation as a probe of reaction mechanism. Synthesis and thermal decomposition of 2,3-diazabicyclo[2.1.1]hex-2-enes. *Journal of the American Chemical Society* **1984**, *106* (15), 4211-4217. DOI: 10.1021/ja00327a025.
(62) Allred, E. L.; Smith, R. L. Thermal and photodecomposition studies with the exo- and endo-5-methoxy-2,3-diazabicyclo[2.2.1]hept-2-ene system. *Journal of the American Chemical Society* **1969**, *91* (24), 6766-6775. DOI: 10.1021/ja01052a039.

(63) Chang, M. H.; Dougherty, D. A. Photochemistry of 2,3-diazabicyclo[2.1.1]hex-2-ene. .beta. Carbon-carbon cleavage to a stereorandom triplet biradical. *Journal of the American Chemical Society* **1982**, *104* (8), 2333-2334. DOI: 10.1021/ja00372a050.
(64) Solomon, B. S.; Thomas, T. F.; Steel, C. Primary processes in the photochemistry of diazabicyclic compounds. *Journal of the American Chemical Society* **1968**, *90* (9), 2249-2258. DOI: 10.1021/ja01011a008.
(65) Adam, W.; García, H.; Martí, V.; Moorthy, J. N.; Peters, K.; Peters, E.-M. Photochemical Denitrogenation of Norbornene-Annelated 2,3-Diazabicyclo[2.1.1]hept-2-ene-Type Azoalkanes: Crystal-Lattice versus Zeolite-Interior Effects. *Journal of the American Chemical Society* **2000**, *122* (14), 3536-3537. DOI: 10.1021/ja994114q.
(66) Steel, C. PHOTOLYSIS OF BICYCLIC AZO COMPOUNDS. I. 2,3-DIAZABICYCLO[2.2.1]2-HEPTENE. *The Journal of Physical Chemistry* **1963**, *67* (9), 1779-1781. DOI: 10.1021/j100803a008.
(67) Thomas, T. F.; Steel, C. Photoinitiation of Unimolecular Reactions. The Photolysis of 2,3-Diazabicyclo[2.2.1]hept-2-ene. *Journal of the American Chemical Society* **1965**, *87* (23), 5290-5293. DOI: 10.1021/ja00951a005.
(68) Thomas, T. F.; Sutin, C. I.; Steel, C. Distribution and exchange of excess vibrational energy produced in the photolysis of 2,3-diazabicyclo[2.2.1]-hept-2-ene. *Journal of the American Chemical Society* **1967**, *89* (20), 5107-5115. DOI: 10.1021/ja00996a004.
(69) Engel, P. S. Sensitized photolysis of a bicyclic azo compound in solution. *Journal of the American Chemical Society* **1969**, *91* (25), 6903-6907. DOI: 10.1021/ja01053a002.
(70) Engel, P. S.; Steel, C. Photochemistry of aliphatic azo compounds in solution. *Accounts of Chemical Research* **1973**, *6* (8), 275-281. DOI: 10.1021/ar50068a004.
(71) Adam, W.; Doerr, M. Wagner-Meerwein rearrangements of radical cations generated by triphenylpyrylium tetrafluoroborate photosensitized electron transfer of azoalkanes. *Journal of the American Chemical Society* **1987**, *109* (5), 1570-1572. DOI: 10.1021/ja00239a048.
(72) Adam, W.; Diedering, M. Enhanced formation of inverted housane through steric effects by rotationally unsymmetric bridgehead substituents in the ring closure of triplet cyclopentane-1,3-diyl diradicals, generated photolytically from 2,3-diazabicyclo[2.2.1]heptene(DBH)-type azoalkanes. *Photochemical & Photobiological Sciences* **2003**, *2* (4), 393-397. DOI: 10.1039/b211319h.
(73) Roth, W. H.; Martin, M. Zur stereochemie der 1.2-cycloaddition an das bicyclo[2.1.0]system. *Tetrahedron Letters* **1967**, *8* (47), 4695-4698. DOI: https://doi.org/10.1016/S0040-4039(01)89583-6.
(74) Adam, W.; Denninger, U.; Finzel, R.; Kita, F.; Platsch, H.; Walter, H.; Zang, G. Comparative study of the pyrolysis, photoinduced electron transfer (PET), and laser-jet and 185-nm photochemistry of alkyl-substituted bicyclic azoalkanes. *Journal of the American Chemical Society* **1992**, *114* (13), 5027-5035. DOI: 10.1021/ja00039a012.
(75) Adam, W.; Grüne, M.; Diedering, M.; Trofimov, A. V. Temperature and Viscosity Dependence in the Stereoselective Formation of the Inverted Housane for the Photochemical Nitrogen Loss from the Deuterium-Stereolabeled Parent Diazabicyclo[2.2.1]hept-2-ene. *Journal of the American Chemical Society* **2001**, *123* (29), 7109-7112. DOI: 10.1021/ja005887d.
(76) Adam, W.; Diedering, M.; Trofimov, A. V. Solvent effects in the photodenitrogenation of the azoalkane diazabicyclo[2.2.1]hept-2-ene: viscosity- and polarity-controlled stereoselectivity in housane formation from the diazenyl diradical. *Physical Chemistry Chemical Physics* **2002**, *4* (6), 1036-1039. DOI: 10.1039/b110562k.
(77) Adam, W.; Diedering, M.; Sajimon, M. C.; Trofimov, A. V. Structural dependence on the stereoselective formation of inverted housane in the viscosity-controlled photodenitrogenation of DBH-type azoalkanes. *Physical Chemistry Chemical Physics* **2003**, *5* (2), 329-332. DOI: 10.1039/b209182h.
(78) Adam, W.; Sajimon, M. C.; Trofimov, A. V. Viscosity-dependent diastereoselectivity and product selectivity in the photodenitrogenation of a spirocyclopropane-substituted, DBH-type azoalkane. *Photochem Photobiol Sci* **2003**, *2* (6), 677-680. DOI: 10.1039/b212531e.

(79) Adam, W.; Diedering, M.; Trofimov, A. V. Intriguing double-inversion stereochemistry in the denitrogenation of 2,3-diazabicyclo[2.2.1]heptene-type azoalkanes: a model mechanistic study in physical organic chemistry. *Journal of Physical Organic Chemistry* **2004**, *17* (8), 643-655. DOI: 10.1002/poc.834.
(80) Trofimov, A. V. Stereochemical inversion upon denitrogenation of electronically excited cycloazoalkanes in viscous media as a function of the reagent structure. *Doklady Chemistry* **2007**, *417* (1), 264-266. DOI: 10.1134/s001250080711002x.
(81) Adams, J. S.; Weisman, R. B.; Engel, P. S. Photodissociation of a bicyclic azoalkane: time-resolved coherent anti-Stokes Raman spectroscopy studies of vapor-phase 2,3-diazabicyclo[2.2.1]hept-2-ene. *Journal of the American Chemical Society* **1990**, *112* (25), 9115-9121. DOI: 10.1021/ja00181a013.
(82) Yamamoto, N.; Olivucci, M.; Celani, P.; Bernardi, F.; Robb, M. A. An MC-SCF/MP2 Study of the Photochemistry of 2,3-Diazabicyclo[2.2.1]hept-2-ene: Production and Fate of Diazenyl and Hydrazonyl Biradicals. *Journal of the American Chemical Society* **1998**, *120* (10), 2391-2407. DOI: 10.1021/ja971733v.
(83) Sinicropi, A.; Page, C. S.; Adam, W.; Olivucci, M. Computational Study on the Origin of the Stereoselectivity for the Photochemical Denitrogenation of Diazabicycloheptene. *Journal of the American Chemical Society* **2003**, *125* (36), 10947-10959. DOI: 10.1021/ja0263137.
(84) Abreha, B. G.; Agarwal, S.; Foster, I.; Blaiszik, B.; Lopez, S. A. Virtual Excited State Reference for the Discovery of Electronic Materials Database: An Open-Access Resource for Ground and Excited State Properties of Organic Molecules. *J Phys Chem Lett* **2019**, *10* (21), 6835-6841. DOI: 10.1021/acs.jpclett.9b02577 From NLM PubMed-not-MEDLINE.
(85) Rollins, N.; Pugh, S. L.; Maley, S. M.; Grant, B. O.; Hamilton, R. S.; Teynor, M. S.; Carlsen, R.; Jenkins, J. R.; Ess, D. H. Machine Learning Analysis of Direct Dynamics Trajectory Outcomes for Thermal Deazetization of 2,3-Diazabicyclo[2.2.1]hept-2-ene. *J Phys Chem A* **2020**, *124* (23), 4813-4826. DOI: 10.1021/acs.jpca.9b10410.
(86) Chen, H.; Li, S. CASPT2//CASSCF Study on the Photolysis Mechanism of 2,3-Diazabicyclo[2.1.1]hex-2-ene: α C−N versus β C−C Cleavage. *The Journal of Organic Chemistry* **2006**, *71* (24), 9013-9022. DOI: 10.1021/jo0611622.
(87) Yagi, S.; Hiraga, Y.; Takagi, R.; Abe, M. Stereochemical deuterium-labeling study on the denitrogenation of 7,7-diethoxy-2,3-diazabicyclo[2.2.1]hept-2-ene. *Journal of Physical Organic Chemistry* **2011**, *24* (10), 894-901. DOI: 10.1002/poc.1872.
(88) Li, J.; Stein, R.; Lopez, S. A. A Theoretical Stereoselectivity Model of Photochemical Denitrogenations of Diazoalkanes Toward Strained 1,3-Dihalogenated Bicyclobutanes. *J Org Chem* **2021**, *86* (5), 4061-4070. DOI: 10.1021/acs.joc.0c02905 From NLM PubMed-not-MEDLINE.
(89) Malmqvist, P.-Å.; Roos, B. O. The CASSCF state interaction method. *Chemical Physics Letters* **1989**, *155* (2), 189-194. DOI: https://doi.org/10.1016/0009-2614(89)85347-3.
(90) Pierloot, K.; Dumez, B.; Widmark, P.-O.; Roos, B. O. Density matrix averaged atomic natural orbital (ANO) basis sets for correlated molecular wave functions. *Theoretica chimica acta* **1995**, *90* (2), 87-114. DOI: 10.1007/BF01113842.
(91) Chai, J.-D.; Head-Gordon, M. Long-range corrected hybrid density functionals with damped atom–atom dispersion corrections. *Physical Chemistry Chemical Physics* **2008**, *10* (44), 6615-6620, 10.1039/B810189B. DOI: 10.1039/B810189B.
(92) Kendall, R. A.; Dunning, T. H., Jr.; Harrison, R. J. Electron affinities of the first-row atoms revisited. Systematic basis sets and wave functions. *The Journal of Chemical Physics* **1992**, *96* (9), 6796-6806. DOI: 10.1063/1.462569 (accessed 10/10/2023).
(93) Shiozaki, T.; Győrffy, W.; Celani, P.; Werner, H.-J. Communication: Extended multi-state complete active space second-order perturbation theory: Energy and nuclear gradients. *The Journal of Chemical Physics* **2011**, *135* (8). DOI: 10.1063/1.3633329 (accessed 3/2/2024).
(94) Tully, J. C. Molecular dynamics with electronic transitions. *The Journal of Chemical Physics* **1990**, *93* (2), 1061-1071. DOI: 10.1063/1.459170 (accessed 4/29/2025).

(95) Hammes-Schiffer, S.; Tully, J. C. Proton transfer in solution: Molecular dynamics with quantum transitions. *The Journal of Chemical Physics* **1994**, *101* (6), 4657-4667. DOI: 10.1063/1.467455 (accessed 7/1/2024).
(96) Granucci, G.; Persico, M. Critical appraisal of the fewest switches algorithm for surface hopping. *The Journal of Chemical Physics* **2007**, *126* (13). DOI: 10.1063/1.2715585 (accessed 4/29/2025).
(97) Aquilante, F.; Autschbach, J.; Baiardi, A.; Battaglia, S.; Borin, V. A.; Chibotaru, L. F.; Conti, I.; De Vico, L.; Delcey, M.; Fdez Galvan, I.; et al. Modern quantum chemistry with [Open]Molcas. *J Chem Phys* **2020**, *152* (21), 214117. DOI: 10.1063/5.0004835.
(98) Fdez. Galván, I.; Vacher, M.; Alavi, A.; Angeli, C.; Aquilante, F.; Autschbach, J.; Bao, J. J.; Bokarev, S. I.; Bogdanov, N. A.; Carlson, R. K.; et al. OpenMolcas: From Source Code to Insight. *Journal of Chemical Theory and Computation* **2019**, *15* (11), 5925-5964. DOI: 10.1021/acs.jctc.9b00532.
(99) Li, J.; Lopez, S. A. A Look Inside the Black Box of Machine Learning Photodynamics Simulations. *Acc Chem Res* **2022**, *55* (14), 1972-1984. DOI: 10.1021/acs.accounts.2c00288.
(100) Li, J.; Reiser, P.; Boswell, B. R.; Eberhard, A.; Burns, N. Z.; Friederich, P.; Lopez, S. A. Automatic discovery of photoisomerization mechanisms with nanosecond machine learning photodynamics simulations. *Chem Sci* **2021**, *12* (14), 5302-5314. DOI: 10.1039/d0sc05610c.
(101) Li, J.; Stein, R.; Adrion, D. M.; Lopez, S. A. Machine-Learning Photodynamics Simulations Uncover the Role of Substituent Effects on the Photochemical Formation of Cubanes. *J Am Chem Soc* **2021**, *143* (48), 20166-20175. DOI: 10.1021/jacs.1c07725.
(102) Li, J.; Lopez, S. A. Excited-State Distortions Promote the Photochemical 4pi-Electrocyclizations of Fluorobenzenes via Machine Learning Accelerated Photodynamics Simulations. *Chemistry* **2022**, *28* (38), e202200651. DOI: 10.1002/chem.202200651.
(103) Virtanen, P.; Gommers, R.; Oliphant, T. E.; Haberland, M.; Reddy, T.; Cournapeau, D.; Burovski, E.; Peterson, P.; Weckesser, W.; Bright, J.; et al. SciPy 1.0: fundamental algorithms for scientific computing in Python. *Nature Methods* **2020**, *17* (3), 261-272. DOI: 10.1038/s41592-019-0686-2.